Research Article Vol. 13, No. 6 / 1 Jun 2022 / Biomedical Optics Express 3461
Biomedical Optics EXPRESS

Hyperspectral evaluation of vasculature in induced peritonitis mouse models

JOŠT STERGAR,[1,2,*] KATJA LAKOTA,[3,4] MARTINA PERŠE,[5] MATIJA TOMŠIČ,[4,5] AND MATIJA MILANIČ[1,2]

[1] J. Stefan Institute, Jamova cesta 39, 1000 Ljubljana, Slovenia
[2] Faculty of Mathematics and Physics, University of Ljubljana, Jadranska ulica 19, 1000 Ljubljana, Slovenia
[3] FAMNIT, University of Primorska, Glagoljaska 8, 6000 Koper, Slovenia
[4] University Medical Centre, Department of Rheumatology, Vodnikova ulica 62, 1000 Ljubljana, Slovenia
[5] Faculty of Medicine,University of Ljubljana, Vrazov trg 2, 1000 Ljubljana, Slovenia
[*] jost.stergar@ijs.si

Abstract: Imaging of blood vessel structure in combination with functional information about blood oxygenation can be important in characterizing many different health conditions in which the growth of new vessels contributes to the overall condition. In this paper, we present a method for extracting comprehensive maps of the vasculature from hyperspectral images that include tissue and vascular oxygenation. We also show results from a preclinical study of peritonitis in mice. First, we analyze hyperspectral images using Beer-Lambert exponential attenuation law to obtain maps of hemoglobin species throughout the sample. We then use an automatic segmentation algorithm to extract blood vessels from the hemoglobin map and combine them into a vascular structure-oxygenation map. We apply this methodology to a series of hyperspectral images of the abdominal wall of mice with and without induced peritonitis. Peritonitis is an inflammation of peritoneum that leads, if untreated, to complications such as peritoneal sclerosis and even death. Characteristic inflammatory response can also be accompanied by changes in vasculature, such as neoangiogenesis. We demonstrate a potential application of the proposed segmentation and processing method by introducing an abnormal tissue fraction metric that quantifies the amount of tissue that deviates from the average values of healthy controls. It is shown that the proposed metric successfully discriminates between healthy control subjects and model subjects with induced peritonitis and has a high statistical significance.

1. Introduction

In recent years, hyperspectral imaging (HSI) has shown promising results in many different biomedical applications [1]. HSI has its roots in remote sensing [2] and is a combination of imaging and spectroscopy that opens up possibilities for novel contrasts in biomedical imaging, such as light scattering and chemical contrasts. In the past, it has been used to segment organs in the abdominal cavity [1], to study a wide range of pathologies such as melanoma [3] and prostate cancer [4], and for many other novel applications to support medicine and biology [1].

Understanding tissue changes associated with a disease is an important aspect of preclinical studies addressing disease onset and mitigation. One such case is peritonitis, which can cause serious complications in patients receiving peritoneal dialysis (PD). The occurence of peritonitis is a major reason for discontinuation of peritoneal dialysis, resulting in a decreased quality of life for patients [5]. Since peritonitis can lead to peritoneal fibrosis and is a major cause of peritoneal dialysis failure, which can even lead to patient deaths [6], it is important to investigate possible mitigation techniques and identify changes associated with the onset and the progression of the disease [7]. In the scope of this study, a chlorhexidine gluconate (CHX) induced mouse model of peritonitis [5,8,9] was used, along with resolvin D as a method to regulate inflammatory response [10]. Morphological and physiological changes in the CHX animal model include inflammation,

#460288 https://doi.org/10.1364/BOE.460288
Journal © 2022 Received 1 Apr 2022; revised 28 Apr 2022; accepted 8 May 2022; published 18 May 2022

Biomedical Optics EXPRESS

fibroblast proliferation, neoangiogenesis, and collagen fiber production that ultimately lead to fibrosis and peritoneal dysfunction [5,9]. In preclinical studies of peritonitis, the main methods used to assess disease state are visual observation of changes and histological examination [5,8,9]. The former provides an overview of the entire specimen, but lacks the sensitivity to subtle changes in morphology and physiology. Histology, on the other hand, offers excellent insight into microscopic changes, but often overlooks smaller lesion areas due to limited sampling. Biomolecular methods, such as DNA microarray, are also used [11], but lack spatial resolution. Therefore novel methods capable of assessing morphological and physiological changes at larger scales with sufficient spatial resolution are needed. This study focuses on blood parameters and blood vessel architecture because neoangiogenesis and luminal narrowing of arterioles have been reported in some studies [9] and a high statistical significance of blood-related metrics was observed in our previous study [12].

Because changes in blood vessel function and structure are difficult to assess with established imaging and examination methods and often require highly skilled personnel (e.g., Doppler ultrasound), we propose a novel approach that combines hyperspectral imaging and extraction of tissue properties with automated vessel segmentation. Such an approach offers new insights through hybrid vasculature-oxygenation maps and opens opportunities for novel metrics to calculate disease burden.

In this paper, we first present the methodology based on hyperspectral images acquired using a custom developed hyperspectral imaging system. We extract tissue properties from the spectra, namely the volume fractions of oxygenated and deoxygenated blood, and use them to create maps of hemoglobin species. These maps are then automatically segmented and used to generate either composite oxygenation-vasculature maps or binary blood vessel network maps. Using the segmented blood vessels, we propose a novel metric of abnormal tissue fraction calculated from tissue and blood vessel oxygenation. We test the proposed metric with statistical tests to confirm that it can reliably detect the presence of peritonitis, demonstrating its applicability.

2. Methods

2.1. Hyperspectral imaging

Hyperspectral imaging (HSI) is an imaging modality that combines imaging with spectroscopy. The result of HSI is a 3-dimensional dataset, often referred to as a hyperspectral cube, that contains both spectral and spatial information such that a spectrum is available for each spatial pixel. This approach allows for both spatial and spectral analysis.

Our in-house developed hyperspectral pushbroom imaging system [12,13], shown schematically in Fig. 1 was used to perform hyperspectral imaging. Samples were illuminated in a transmission geometry with a halogen light source placed below the sample. Light passing through the sample was collected with a 50 mm objective lens (Xenoplan 2.8/50-0902, Schneider Kreuznach, Germany) coupled to an imaging spectrograph (ImSpector V10e, Specim, Finland) designed to operate in the spectral range between 400 nm and 1000 nm. The diffracted light was recorded using a 5 MP CMOS camera (Blackfly S BFS-U3-51S5M-c, FLIR Integrated Imaging Solutions, Canada) with a detector size of 2/3" and a USB3.0 connection resulting in images with a resolution of 2448×2048 along the spatial and spectral dimensions, respectively. To achieve a better signal-to-noise ratio, the images were binned by a factor of 2 along the spatial dimension, resulting in 1224 pixels across the field of view of approximately 3.7 cm, giving a pixel size of 0.03 mm in the object plane. The actual spatial resolution determined using a USAF target was 0.1 mm, whereas the spectral resolution determined using a HeNe laser line broadening was 2.9 nm.

In addition to the sample measurement, a white reference image was acquired. Here, the light source illuminated the white diffusive plate, which was also used as the substrate for the sample imaging and was located between the light source and the spectrograph. In this way, the only

Biomedical Optics EXPRESS

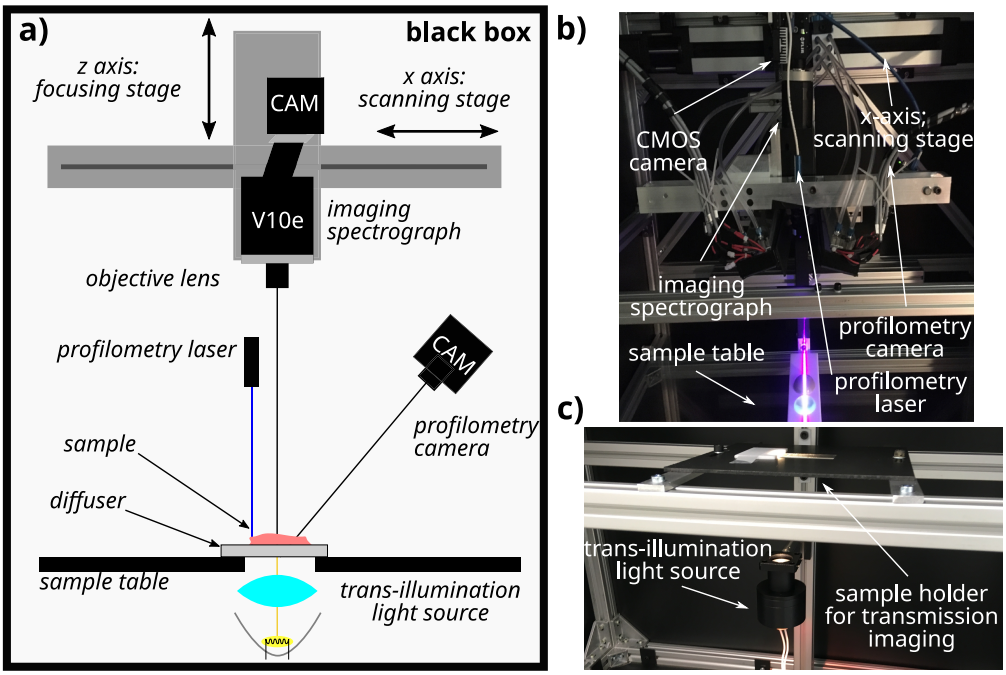

Fig. 1. HSI system schematic. A complete schematic of the HSI system used for this study is shown in a), with the imaged object placed on top of the diffusive plate above the transmission halogen light source. b) depicts the internal components of the system. Components used in the transmission geometry are annotated. In c), the illumination assembly along with the sample table is presented.

difference between the white reference and sample measurements was the absence of the sample in the former. The acquisition protocol was adjusted to minimize the time between sequential acquisition of the reference and sample images to minimize the effects of thermal instability of the imaging system. The dark current of the detector was omitted from the measurements due to an internal camera calibration. The sample data was normalized to obtain the real transmittance values by dividing the recorded sample image with the white reference image. The normalization also corrected the inhomogeneities in the illumination profile.

An integrated laser profilometry system based on laser triangulation [14,15] was used to evaluate the sample thickness. The profilometry system allows imaging of the 3D surface with resolutions of 0.1 mm in the lateral directions and 0.05 mm in the Z direction.

2.2. Study protocol

Mice subjects included in this study were 17 male C57BL/6J mice that were 15-16 weeks old at the beginning of the study (Medical Experimental Centre, Ljubljana, Slovenia). Before the experiment, all necessary approvals were obtained from the National Ethics Committee of the Republic of Slovenia and the Administration of the Republic of Slovenia for Food Safety, Veterinary and Plant Protection (Licence No. 34401-13/2018/5). The experiments were performed in accordance with national and EU legislation (Directive 2010/63/EU). During the study, animals were in a barrier system at 22 – 25 °C, 55 ± 10% humidity, 12 h light/dark cycle (light 7a.m.-7p.m.); SPF according to FELASA recommendations (QM diagnostics, The Netherlands), negative to all tested microorganisms. They were housed in open cages (Ehret, 825 cm^2 floor area) with autoclaved bedding (Lignocel 3/4, Germany) and enrichment (Mouse

Biomedical Optics EXPRESS

house, Tecniplast; paper towels; paper tunnels), maintenance diet (Altromin 1324, Germany), and autoclaved water (bottles, Tecniplast) *ad libitum*.

The treated model group received all the substances in the study. Peritonitis was induced by intraperitoneal injection (G33) of 200 μL of chlorhexidine gluconate - CHX solution (0.1% CHX (Wako Pure Chemical Industries) in 15% ethanol in phosphate buffered saline - PBS) per mouse every second day. In addition, this group received resolvin D1 or epiresolvin D1 (an omega 3-fatty acid metabolite dissolved in absolute ethanol (100 ng/μL), Cayman Chemical, USA) daily resolvin solution (100 ng dissolved in PBS, injected as 100 μL per mouse) as a treatment strategy. In the (untreated) model and the (untreated) control groups, the daily resolvin solution injection was replaced by 1% ethanol dissolved in PBS. In treated control and (untreated) control groups, CHX solution injections used to initiate the model were replaced by PBS injections. In this way, the amount of physical damage due to the injections was equal for all the experimental groups. The entire protocol along with the group abbreviations and nomenclature used throughout this paper is shown in Table 1. Because the distinction between the two resolvins was not important in the scope of this study, both groups that received different resolvins are analyzed together. The subjects included in this study were a subset of subjects in a larger study who were selected for participation based on available imaging dates when the addition of hyperspectral imaging of the subjects was a minimal intrusion into the established workflow.

Table 1. Three week experiment cohort overview. Overview of the mice groups and the intraperitoneally injected substances for each group on odd and even days are given in the first table. The whole cohort consisted of n = 17 subjects. Column marked with # lists number of subjects in each group. In the second table, substances administered are listed. Legend: CHX - chlorhexidine gluconate.

Abbreviation	Group	Even days	Odd days	#
PBS	control	PBSE	PBS+PBSE	2
PBS+RVD	treated c.	RVD	PBS+RVD	6
CHX	model	PBSE	CHX+PBSE	3
CHX+RVD	treated m.	RVD	CHX+RVD	6

Abbreviation	Substance	Injected volume
PBS	PBS	200 μL
PBSE	1% ethanol in PBS	100 μL
RVD	resolvin D1 in PBS	100 μL
CHX	0.1% CHX in 15% ethanol in PBS	200 μL

The 17 subjects in the experimental cohort were treated for three weeks prior to the sacrifice. After euthanasia by CO_2-gas inhalation, the abdominal cavity was filled with 6.5 mL of ice cold PBS. After 30 seconds of gentle massage, PBS was removed to collect cells for further analysis. The skin was removed and the abdominal wall was opened along the *linea alba* from the xiphoid cartilage to the pelvic opening. One half of the abdominal wall, divided by the *linea alba*, was excised, placed on a white Plexiglas substrate, and imaged in transmission geometry using the hyperspectral imaging system.

The study was conducted as a double-blind study in which neither the person performing the final phase of the experiment nor the person processing the data knew which group the subjects belonged to. In this way, potential bias was minimized. Subjects were imaged in a random order to further minimize the possibility of observer bias. The data collection protocol was established before the study began, while the analysis protocol was established after data collection. The

Biomedical Optics EXPRESS

work presented is in the development and exploration phase, which roughly corresponds to IDEAL phases 2a and 2b [16].

2.3. Extraction of physiological parameters

To extract physiological parameters, namely oxygenated and deoxygenated blood volume fraction along with the blood oxygenation, a simple, yet fast model was used. To approximate the scattering in the tissue, a common power law was used in the form of [17]

$$\mu_s' = a\left(\frac{\lambda}{500\ \text{nm}}\right)^{-b}, \tag{1}$$

where parameter a is the value of the reduced scattering coefficient at 500 nm and b is the scattering power.

Light absorption in the tissue was modelled by considering both hemoglobin species and weighting them by the blood volume fractions BVF

$$\mu_a = BVF_O\mu_{a,oxy} + BVF_D\mu_{a,deoxy}, \tag{2}$$

where BVF_O and BVF_D are the blood volume fractions of oxygenated and deoxygenated blood, respectively. Data for the absorption coefficients of pure oxygenated and deoxygenated blood $\mu_{a,oxy}$ and $\mu_{a,deoxy}$ were obtained from the literature [18] and corrected for mice gene line specified hematocrit of 51.2%.

Light attenuation in tissue was modelled using the Beer-Lambert exponential attenuation law [19]

$$T = \frac{I}{I_0} = e^{-(\mu_s'+\mu_a)d}, \tag{3}$$

where T is the normalized transmittance as the ratio of the transmitted intensity I and the incident intensity I_0, d is the sample thickness and μ_s' and μ_a are reduced scattering and absorption coefficients, respectively.

A nonlinear least squares *lsqnonlin* fitting routine in MATLAB (MathWorks, USA) was used to fit the above model equations to the white reference normalized hyperspectral data and to determine the blood volume fractions for both hemoglobin species. The fitted parameters were the oxygenated and deoxygenated blood volume fractions BVF_O and BVF_D, along with the scattering parameters a and b. The thickness of the sample d was determined from the laser profilometry measurements. The calculated blood volume fractions were also used to calculate the total blood volume fraction $BVF = BVF_O + BVF_D$ and the oxygenation $SpO_2 = BVF_O/BVF$. The resulting maps for the blood-related tissue properties are shown along with an RGB projection of the hyperspectral cube in Fig. 2. The RGB projection of HSI was obtained by multiplication of the normalized tissue spectra by CIE XYZ tristimulus spectra [20]. The results were summed over the entire wavelength range, and finally normalized by the number of wavelengths. In this way, each transmittance spectrum was translated into the three CIE XYZ colorspace coordinates. To obtain the RGB image representation from the XYZ colorspace, a MATLAB function *xyz2rgb* was used with the default option of the D65 standard illuminant.

2.4. Automatic vessel segmentation

To obtain maps of blood vessels from blood parameter maps, automatic segmentation of blood vessels was performed. Before segmenting the vessels, the contrast of the BVF image was enhanced using CLAHE adaptive histogram equalization implemented as *adapthisteq* function in MATLAB. This step produces a high-contrast image (Fig. 3(a)), but destroys the quantitative information. The image was additionally padded to mitigate artifacts that may occur at the edges of the image.

Biomedical Optics EXPRESS

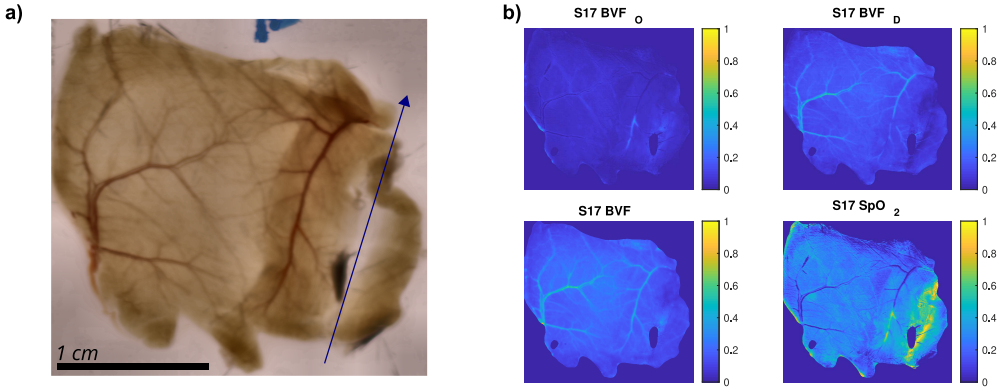

Fig. 2. RGB projection and fit results. Locally contrast enhanced RGB projection of the HSI is shown in panel a). The shaft of the blue arrow marks the location of *linea alba* and the direction points towards the head. Peritoneal side of the abdominal wall is facing the camera. In panel b), parameters fitted with the model relating to the blood are shown. Treated control group subject S17.

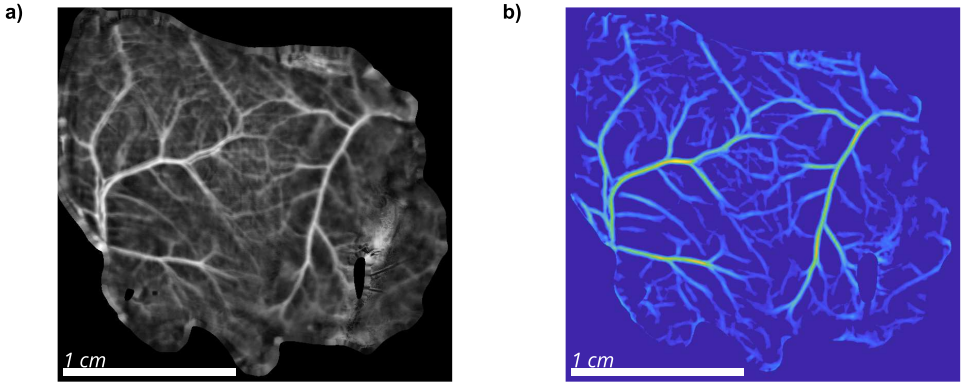

Fig. 3. Enhanced BVF total and B-COSFIRE images. Panel a) shows CLAHE enhanced BVF_T map as obtained from the model. Additionally, map is padded by extending border values to avoid effects of the border on automatic segmentation. In panel b), enhanced B-COSFIRE image is shown. Treated control group subject S17.

Biomedical Optics EXPRESS

To automatically detect the linear structural features corresponding to blood vessels, an unsupervised filtering algorithm B-COSFIRE [21–23] was used. Briefly, this filter uses difference-of-gaussian (DoG) functions (Fig. 4(a)) arranged along a line (Fig. 4(b)) and performs a convolution with the original image to enhance linear features. Individual filter is parameterized by the distances of the DoGs from the support center ρ and the widths of the DoGs σ. Several such filters are then applied at different rotations parameterized by the angle ϕ. The algorithm uses additional parameters *length*, which specifies the length of the linear segments to be detected, and parameters σ_0 and α, which specify the blur that allows small deviations from the perfectly linear feature. Since a symmetric line, as defined in Fig. 4, fails to amplify line endings, an additional asymmetric filter is introduced containing i.e.only DoG2 and DoG4. More information about the algorithm can be found in the original papers by Azzopardi, Strisciuglio, and others [21–23]. The filter parameters used for this work were determined by manually testing different parameters to obtain a robust set and are listed in Table 2.

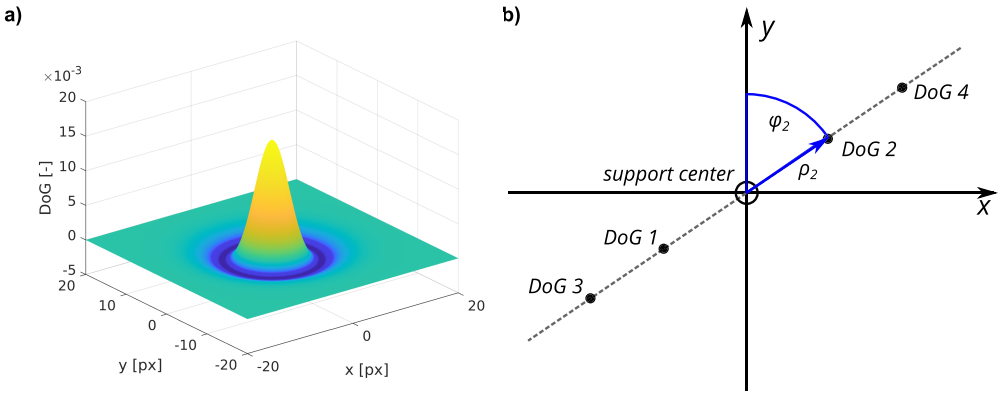

Fig. 4. B-COSFIRE filtering uses a set of difference-of-gaussian (DoG) functions (a) arranged along a linear segment, as shown in b).

Table 2. B-COSFIRE filter parameters for blood vessel segmentation. Parameters for both filters used in automatic segmentation are given in the table. Length denotes the length of a line segment to be detected, whereas orientations denotes the number of orientations used to achieve rotational invariance. Parameters depend on image resolution and sample characteristics, such as expected vessel dimensions and lengths. All units are in pixels.

parameter	symmetric filter	asymmetric filter
σ	5.5	4.0
ρ	2	2
length	20	20
orientations	12	24
σ_0	3	4
α	0.7	0.1

After the B-COSFIRE operation, the resulting image was first cropped to the original size, removing slightly more than was added in the padding step, further eliminating possible artefacts

Biomedical Optics EXPRESS

at the image or sample edge. A threshold was also applied to the processed image to remove the background. Small spurious unconnected areas were removed using *bwareaopen* MATLAB function that eliminated areas smaller than 150 pixels. Filtered segmented image was smoothed using a 2-D Gaussian filtering, implemented in MATLAB as *imgaussfilt* function, with the default standard deviation parameter of 0.5 pixels and kernel size of 3 pixels. This has minimal effect on the overall image but removes sharp edges that can cause problems when using the segmentation for Fourier analysis. The resulting segmentation of blood vessels for subject S17 is shown in Fig. 3(b).

From the B-COSFIRE filter response, binary vasculature maps were obtained by applying another threshold to the images. The resulting raw binary mask (Fig. 5(a)) contained some small artefacts that were a consequence of the segmentation and needed to be removed. These regions were removed by using the MATLAB function *bwareaopen* that removed all areas smaller than 100 pixels in surface. The resulting filtered image is shown in Fig. 5(b). In addition, a skeleton of the vascular tree was calculated from the filtered image using the *bwskel* function in MATLAB. To avoid accidentally unconnected vessels, the skeletonized image was dilated by 3 pixels using the *imdilate* function and a diamond structural element. The resulting skeleton in Fig. 5(c) could be further used to evaluate the structure of the vascular network.

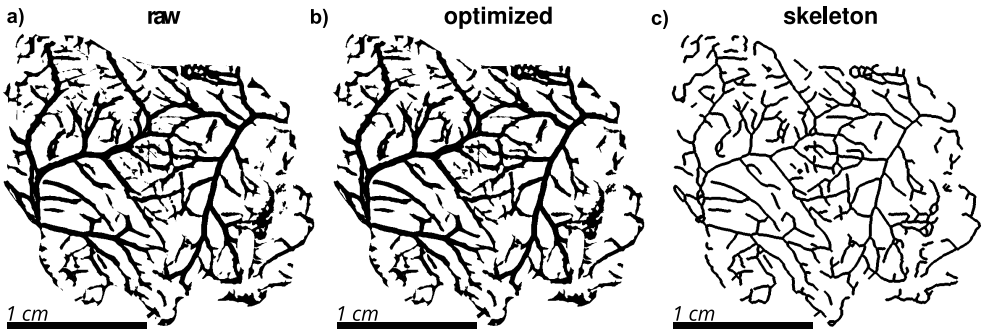

Fig. 5. Automatic binary segmentation of blood vessels. Panel a) shows raw output obtained by thresholding the B-COSFIRE image. In panel b), small areas are removed and vessels are slightly dilated to remove any artificial termination of the segmented vessels. In panel c), a skeleton of segmented vessels is obtained. Treated control group subject S17.

3. Results

Blood vessels were first visually examined by superimposing the oxygenation map over the B-COSFIRE segmentation. For this purpose, an unmodified oxygenation map with an additional opacity channel was plotted. Filtered segmentation was used for the opacity channel. This process consequently provides smoother images due to the smoothing during the generation of the segmented image and by gradually changing from fully opaque to a fully transparent image at the edges of the vessels. In this way, a composite map of oxygenation and vessel architecture was created. Two example maps are shown in Fig. 6. Since the method is not depth resolved, the oxygenation of blood in the vessels reported in this paper is actually a combination of oxygenation of the blood in the segmented vessels and in the tissue above and below the vessels. Since most of the blood is located in the segmented vessels, total oxygenation of the sample at points with vessels still provides a good approximation of the oxygenation of the blood in the segmented vessels themselves. Please note, that due to the protocol including CO_2 euthanasia, no differentiation between arteries and veins could be made. The image thus shows all vessels that were filled with blood during the imaging. At first glance, the images of the

Biomedical Optics EXPRESS

healthy control group subject S30 (a) and the diseased model group subject S21 (b) appear similar, but subtle differences can be seen in the peripheral regions. In particular, the diseased subjects showed increased oxygenation in the peripheral part of the tissue (regions marked with green dashed ellipses), as indicated by the redder smaller vessels. An interesting abnormality, indicated by a white arrow in Fig. 6(a), was observed in some of the subjects as a high increase in oxygenation of blood in larger vessels. This appears as if an occluded blood vessel was not filled with deoxygenated blood during the sacrifice. These vessels occur in the areas near the *linea alba* (marked with a gray line in Fig. 6) and thus could be due to the blood vessels damaged during the application of the intraperitoneal injections.

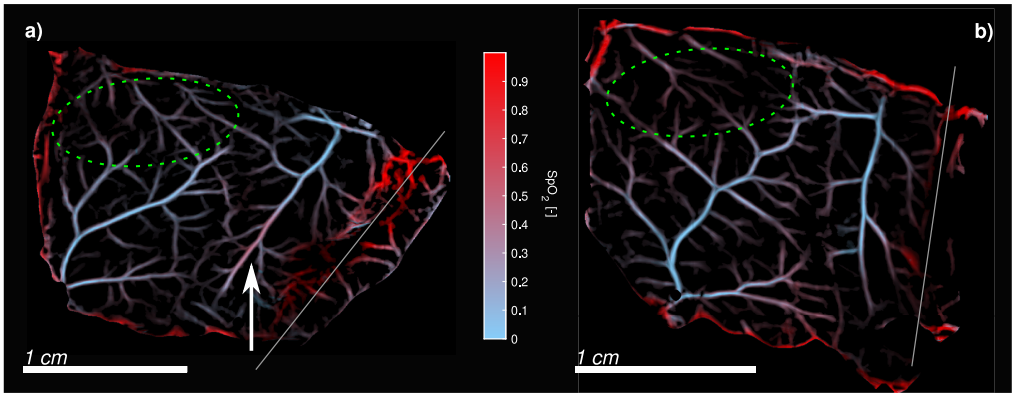

Fig. 6. Vasculature oxygenation image. Oxygenation in vasculature is plotted by using only the B-COSFIRE segmented vessels to obtain a map of vasulature and the oxygenation. In panel a) a control group S30 subject is displayed whereas in panel b) a model subject S21 is plotted. A possibly obstructed blood vessel in an otherwise healthy subject is marked by a white arrow. Green dashed ellipse marks the peripheral area with visible differences in oxygenation between both subjects and the gray line denotes the line alba.

Qualitative differences observed visually from oxygenation maps were further analyzed to obtain quantitative metrics and potentially relate them to disease severity. First, oxygenation information was divided into blood vessels and surrounding tissue based on the binary segmentation maps shown in Fig. 5(b). The data obtained in this fashion was plotted as a per-image histogram, with an example shown in Fig. 7(a). A difference between oxygenation in vessels and tissue was observed with lower values for vessels. This finding is consistent with the protocol involving CO_2 euthanasia, which significantly decreases the oxygen saturation of blood circulating in the vessels. Second, an increase in the mode (most frequent value) of the oxygenation was observed in the model subjects both in vessels and in the surrounding tissue. This change is shown in the scatter plot for both oxygenation modes in Fig. 7(b). In this figure, a large difference can be seen between the model (CHX & CHX+RVD) and control (PBS & PBS+RVD) groups.

Considering only the mode of oxygenation as in Fig. 7(b), some subjects (subject S25) would be mis-classified as diseased. To avoid this, the relative abnormal fraction metric was introduced. First, the value of 0.35 oxygenation was selected based on the Fig. 7(b) and used as a threshold between healthy and diseased tissue. Further, this value was used to calculate the relative fraction of tissue and vessels with oxygenation above this threshold. The relative abnormal fraction metric is thus related to the surface area of tissue exhibiting abnormal oxygenation. The metric is defined as

$$RAF = \frac{N_{SpO_2>0.35}}{N_{all}}, \tag{4}$$

Biomedical Optics EXPRESS

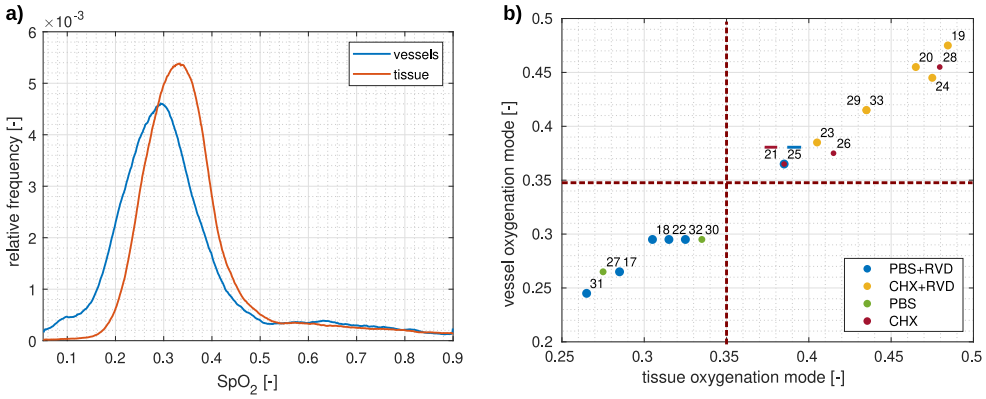

Fig. 7. In a), a smoothed histogram of oxygenation in vessels and in the surrounding tissue for a healthy subject S30 is shown. Integral of the histogram (1000 bins) is normalized to unity. In b), a scatter plot of most frequent values of histograms (mode) for the whole population of both vessel and surrounding tissue oxygenation is displayed. Each node, marked with the sequential number of the subject in the study represents a single animal. With a maroon line, value of $SpO_2 = 0.35$ is denoted. Where groups of subjects are not obvious from label placement, additional colored line above the number indicates the appropriate group.

where RAF is the relative abnormal fraction, $N_{SpO_2>0.35}$ is the number of pixels with increased oxygenation, and N_{all} is the number of all pixels included in the analysis. The results of this metric for blood vessels and surrounding tissue are shown in Fig. 8(a) and (b), respectively.

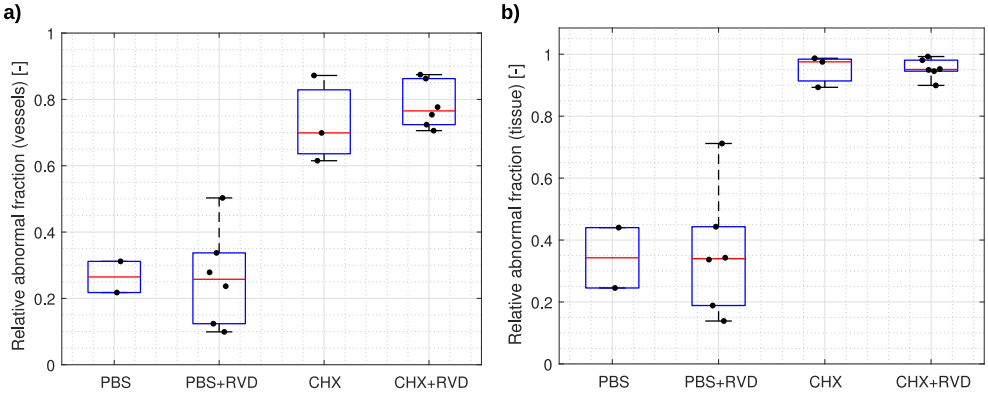

Fig. 8. Box plots of relative abnormal fraction (RAF) metric for vessels (a) and surrounding tissue (b). Individual subjects are denoted by points. Red line shows the median, box covers the interquartile range and whiskers show maximal and minimal values.

From the box plots in Fig. 8 (per-subjects bar chart is available in the Supplement 1), there is a clear difference between control group subjects (PBS & PBS+RVD groups) and model group subjects (CHX & CHX+RVD groups). In general, less than half of the tissue exhibited oxygenation higher than the set threshold in the control groups whereas in the model groups, the relative abnormal fractions approached 1. This suggests widespread changes in the tissue due to the prolonged inflammation. No significant differences were observed between the resolvin treated and untreated groups, neither for the vessels nor for the surrounding tissue. To test this, a two-sided Wilcoxon test implemented as *ranksum* function in MATLAB was used, providing

Biomedical Optics EXPRESS

the values for CHX and CHX+RVD of $p = 0.38$ and $p = 1$ for vessels and surrounding tissue, respectively. For PBS and PBS+RVD groups, $p = 1$ was obtained for the both vessels and the surrounding tissue. These findings indicate, that both resolvin (RVD) receiving groups were statistically indistinguishable from those without resolvin.

To further test the statistical power of the proposed relative abnormal fraction *RAF* metric, an analysis of statistical significance using a Wilcoxon rank-sum test in Matlab was performed. To determine the effect of the proposed threshold for oxygenation on classification, significance was evaluated at different thresholds for oxygenation, as shown in Fig. 9(a). Differences with high statistical significance ($p<0.01$) were observed almost independently of the threshold value. This observation is supported by the visually dramatically different histograms of a healthy and diseased subjects (see Fig. 9(b)).

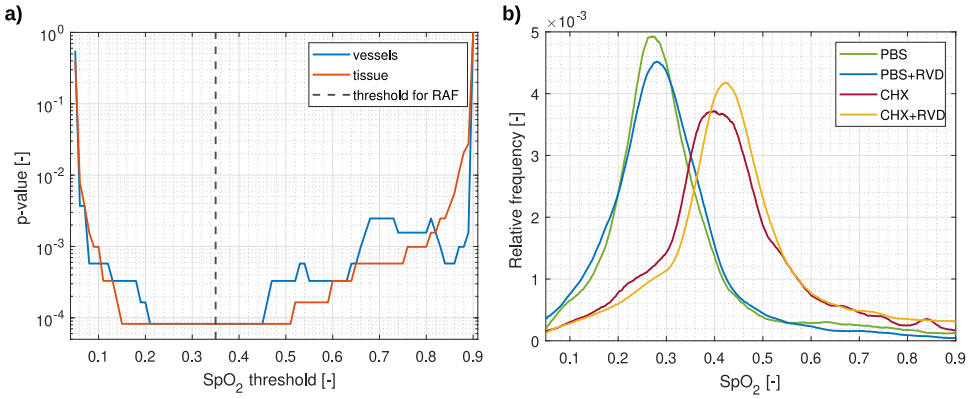

Fig. 9. Evaluation of statistical significance of the proposed relative abnormal fraction of tissue and blood vessels in relation to the oxygenation threshold (a). Dashed black line shows the threshold value selected for relative abnormal fraction (RAF) metric. Example average histograms for blood vessel oxygenation of a healthy and diseased subjects, showing marked differences (b).

4. Discussion

The tissue property extraction model was found to be suitable for determining blood volume fractions and hemoglobin oxygenation in this study, as confirmed by the statistically significant results of the double-blind study. However, the use of both the power law approach to model reduced scattering and Beer-Lambert's law inherently introduce some uncertainty in the absolute values of the scattering parameters (scattering a and b) and in the hemoglobin concentration obtained from this model [24]. The use of Beer's law is justified to some extent by the fact that the samples were rather thin and translucent. However, the use of the combination of the two simple models introduces a large uncertainty in determining the exact scattering properties of the tissue, which were therefore excluded from further analysis. In addition, oxygenation values were used to classify subjects, which should be more robust than absolute values of blood volume fractions. In the future, a more robust model of light propagation in tissue could be used that would also provide more reliable absolute values. An example would be the adding-doubling algorithm [19,25,26], which would also allow extraction of tissue scattering properties and provide better insight into tissue morphology changes.

The main parameters observed in this study were the structure of the vascular network and the oxygenation of the blood therein. The oxygenation of the blood in the vessels was approximated for the scope of this study by the overall oxygenation of the blood in the parts of the tissue where segmented vessels were present. This approach could offset the values because the regions above

Biomedical Optics EXPRESS

and below the segmented vessels also contribute to the total oxygenation. These effects are limited by the fact that a) most of the blood is in the segmented vessels, and b) that the samples were thin and the segmented vessels subsided a considerable proportion of the total tissue. In the future, these effects could be reduced by calculating the segmented vessel diameter from the observed projection and subtracting the contribution of tissue above and below these vessels. The latter could be estimated from the pixels surrounding the segmented vessels. Because no systematic differences in oxygenation were observed within the different vessels, it was not possible to determine whether the vessels were veins or arteries. This is mainly due to the protocol involving CO_2 euthanasia, which causes an inrush of deoxygenated blood first into the arterial network. In studies in which such differentiation would be required, an additional experimental step could be introduced. One possible approach would be to use a method capable of detecting blood movement within the vessels in-vivo, such as Doppler OCT [27], and then coregister the images to separate arteries from veins. This step could allow the creation of a blood vessel atlas. Such an atlas could later be used to decouple arteries and veins based on their relative location and architecture even without the additional imaging step. Analysis of tissue and vascular oxygenation revealed statistically significant differences between healthy and diseased experimental groups, leading to the introduction of a successful relative abnormal fraction. In addition, a study of the blood vessel network with fractal dimensions [28,29] was also performed but yielded null results. First, the non-binarized vasculature maps were used to calculate the Fourier fractal dimension [30] since such approach has been successful in several studies on biological samples [31–33]. In this study, no significant differences were found between healthy and diseased subjects in fractal dimensions calculated with the Fourier transform. Skeletonized vascular maps were additionally used in calculation of the box-counting fractal dimension [28], but again the results showed no statistically significant differences between the experimental groups. Additional visual inspection of the vessel maps revealed no significant differences in vascular architecture between subjects in the different groups, confirming the results of the fractal dimension analysis. On the basis of these observations, two conclusions suggest themselves: a) the resolution of the imaging modality was not sufficient to observe the growth of new, small blood vessels, or b) there was no new growth or no change in the topology of the vascular network. In the future, the approach could be extended to study various pathologies with proven neovascularization, providing an additional metric to assess disease progression. It is important to note that the presented results show, that even with lower resolution, it is possible to detect the tissue changes that accompany peritonitis. Additionally, the null results for the vasculature architecture analysis place the minimum resolution and disease induction time for these changes to be visible in the given animal model above those used in this experiment.

The metrics based on oxygenation, although highly statistically significant, also lend themselves to future study from a biological standpoint. Although it is evident that statistically significant changes are occurring, the biological reasons for the observed changes are not entirely clear at this time. A single study in the literature suggests a possible luminal narrowing of the arterioles [9], but the results are not adequately investigated and discussed. To better understand these changes, the protocol and nature of the disease will be further investigated in the future. Changes in oxygenation can be grossly attributed to changes in oxygenation before sacrifice but could also be a consequence of different vessel and tissue permeability as euthanasia was performed with CO_2 gas, which naturally reduces oxygenation. The latter is consistent with results from other studies [9].

Recently, machine learning approaches to image segmentation and classification have been gaining popularity in many different areas of biomedical optics [34] as well as in general medical physics for computer-aided recognition [35]. Artificial intelligence methods present promising results, from improvements of optical methods and segmentation of optical images [34], help with segmentation of medical images [36], to automatically classifying and screening

Biomedical Optics EXPRESS

of cancer [37,38], among others. In the future, the segmentation task could be delegated to machine learning, reducing processing time and user's work in setting appropriate filter parameters. It has already been shown that machine learning approaches can provide good results in blood vessel segmentation [39,40]. Nonetheless, the presented approach addresses the need to generate a wealth of training data and thus represents a key component in the development of a machine learning approach for segmentation and generation of composite oxygenation maps from hyperspectral images.

5. Conclusion

In conclusion, an approach for the generation of composite vasculature maps with oxygenation information form hyperspectral images was presented. The approach based on a simple model of light-tissue interaction and the B-COSFIRE filter enables fast analysis and provides statistically significant results with minimal user interaction. Based on the vascular maps and oxygenation information, a relative metric for abnormal tissue was proposed, implemented, and statistically tested. It showed reliable, highly statistically significant ($p<0.01$) performance in classifying control and model group subjects with and without peritonitis, respectively. In addition, the possibility of creating binary segmentation maps that can be used for blood vessel structure analysis was presented.

The research presented in this work serves as an introduction to a new composite hyperspectral image representation that could be used in the future to further explore oxygenation related changes in biological tissues, and provides a solid foundation for the implementation of advanced machine learning-based approaches to vascular map generation. These, in turn, could help provide new biomarkers of vascular form and function and support clinical and preclinical research.

Funding. Javna Agencija za Raziskovalno Dejavnost RS (J2-8171, P1-0389, P3-0054, P3-0314, J3-3083).

Acknowledgments. Authors would like to acknowledge the help of the Slovenian Society for Rheumatology development.

Disclosures. The authors declare that there are no conflicts of interest related to this article.

Data availability. Data underlying the results presented in this paper are not publicly available at this time but may be obtained from the authors upon reasonable request.

Supplemental document. See Supplement 1 for supporting content.

References

1. G. Lu and B. Fei, "Medical hyperspectral imaging: A review," J. Biomed. Opt. **19**(1), 010901 (2014).
2. A. F. Goetz, G. Vane, J. E. Solomon, and B. N. Rock, "Imaging Spectrometry for Earth Remote Sensing," Science **228**(4704), 1147–1153 (1985).
3. I. Diebele, I. Kuzmina, A. Lihachev, J. Kapostinsh, A. Derjabo, L. Valeine, and J. Spigulis, "Clinical evaluation of melanomas and common nevi by spectral imaging," Biomed. Opt. Express **3**(3), 467 (2012).
4. H. Akbari, L. V. Halig, D. M. Schuster, A. Osunkoya, V. Master, P. T. Nieh, G. Z. Chen, and B. Fei, "Hyperspectral imaging and quantitative analysis for prostate cancer detection," J. Biomed. Opt. **17**(7), 0760051 (2012).
5. Y. Ito, H. Kinashi, T. Katsuno, Y. Suzuki, and M. Mizuno, "Peritonitis-induced peritoneal injury models for research in peritoneal dialysis review of infectious and non-infectious models," Ren. Replace. Ther. **3**(1), 16 (2017).
6. J. Pajek, A. J. Hutchison, S. Bhutani, P. E. Brenchley, H. Hurst, M. P. Perme, A. M. Summers, and A. Vardhan, "Outcomes of Peritoneal Dialysis Patients and Switching to Hemodialysis: A Competing Risks Analysis," Peritoneal Dial. Int. **34**(3), 289–298 (2014).
7. T. Augustine, P. Brown, S. Davies, A. Summers, and M. Wilkie, "Encapsulating peritoneal sclerosis: clinical significance and implications," Nephron Clin. Pract. **111**(2), c149–c154 (2009).
8. R.-P. Lee, C.-J. Lee, Y.-M. Subeq, and B.-G. Hsu, "A model of chlorhexidine digluconate-induced peritoneal fibrosis in rats," Tzu Chi Med. J. **24**(3), 108–115 (2012).
9. Y. Ishii, T. Sawada, A. Shimizu, T. Tojimbara, I. Nakajima, S. Fuchinoue, and S. Teraoka, "An experimental sclerosing encapsulating peritonitis model in mice," Nephrology Dialysis Transplantation **16**(6), 1262–1266 (2001).
10. S. Krishnamoorthy, A. Recchiuti, N. Chiang, G. Fredman, and C. N. Serhan, "Resolvin D1 receptor stereoselectivity and regulation of inflammation and proresolving MicroRNAs," The Am. J. Pathol. **180**(5), 2018–2027 (2012).

Biomedical Optics EXPRESS

11. H. Yokoi, "Pleiotrophin triggers inflammation and increased peritoneal permeability leading to peritoneal fibrosis," Kidney Int. **81**(2), 160–169 (2012).
12. J. Stergar, R. Dolenec, N. Kojc, K. Lakota, M. Perše, M. Tomšič, and M. Milanic, "Hyperspectral evaluation of peritoneal fibrosis in mouse models," Biomed. Opt. Express **11**(4), 1991 (2020).
13. R. Dolenec, L. Rogelj, J. Stergar, and M. Milanic, "Modular multi-wavelength LED based light source for hyperspectral imaging," in *Novel Biophotonics Techniques and Applications V*, A. Amelink and S. K. Nadkarni, eds. (SPIE, 2019), p. 56.
14. U. Pavlovčič, J. Diaci, J. Možina, and M. Jezeršek, "Wound perimeter, area, and volume measurement based on laser 3D and color acquisition," BioMedical Eng. OnLine **14**(1), 39 (2015).
15. L. Rogelj, U. Pavlovčič, J. Stergar, M. Jezeršek, U. Simončič, and M. Milanič, "Curvature and height corrections of hyperspectral images using built-in 3D laser profilometry," Appl. Opt. **58**(32), 9002 (2019).
16. P. McCulloch, D. G. Altman, W. B. Campbell, D. R. Flum, P. Glasziou, J. C. Marshall, and J. Nicholl, "No surgical innovation without evaluation: The IDEAL recommendations," The Lancet **374**(9695), 1105–1112 (2009).
17. S. L. Jacques, "Optical properties of biological tissues: A review," Physics in Medicine and Biology **58**(11), R37–R61 (2013).
18. M. Friebel, J. Helfmann, U. Netz, and M. Meinke, "Influence of oxygen saturation on the optical scattering properties of human red blood cells in the spectral range 250 to 2000 nm," J. Biomed. Opt. **14**(3), 034001 (2009).
19. A. J. Welch and M. J. van Gemert, eds.*Optical-Thermal Response of Laser-Irradiated Tissue* (Springer, Dordrecht, 2011), 2nd ed.
20. T. Smith and J. Guild, "The C.I.E. colorimetric standards and their use," Trans. Opt. Soc. **33**(3), 73–134 (1931).
21. G. Azzopardi, N. Strisciuglio, M. Vento, and N. Petkov, "Trainable COSFIRE filters for vessel delineation with application to retinal images," Med. Image Anal. **19**(1), 46–57 (2015).
22. N. Strisciuglio, G. Azzopardi, M. Vento, and N. Petkov, "Supervised vessel delineation in retinal fundus images with the automatic selection of B-COSFIRE filters," Med. Image Analysis **27**(8), 1137–1149 (2016).
23. N. Strisciuglio and N. Petkov, "Delineation of line patterns in images using B-COSFIRE filters," in *2017 International Conference and Workshop on Bioinspired Intelligence (IWOBI)*, (IEEE, 2017), pp. 1–6.
24. I. Oshina and J. Spigulis, "Beer–Lambert law for optical tissue diagnostics: Current state of the art and the main limitations," J. Biomed. Opt. **26**(10), 1 (2021).
25. S. A. Prahl, M. J. C. van Gemert, and A. J. Welch, "Determining the optical properties of turbid media by using the adding–doubling method," Appl. Opt. **32**(4), 559 (1993).
26. T. Tomanic, L. Rogelj, and M. Milanic, "Robustness of diffuse reflectance spectra analysis by inverse adding doubling algorithm," Biomed. Opt. Express **13**(2), 921–949 (2022).
27. B. Baumann, B. Potsaid, M. F. Kraus, J. J. Liu, D. Huang, J. Hornegger, A. E. Cable, J. S. Duker, and J. G. Fujimoto, "Total retinal blood flow measurement with ultrahigh speed swept source/Fourier domain OCT," Biomed. Opt. Express **2**(6), 1539 (2011).
28. J. C. Russ, *Fractal Surfaces* (Springer, 1994).
29. J. P. Sturmberg and B. J. West, "Fractals in Physiology and Medicine," in *Handbook of Systems and Complexity in Health*, J. P. Sturmberg and C. M. Martin, eds. (Springer New York, 2013), pp. 171–192.
30. M. Z. C. Azemin, D. K. Kumar, T. Y. Wong, R. Kawasaki, P. Mitchell, and J. J. Wang, "Robust methodology for fractal analysis of the retinal vasculature," IEEE Trans. Med. Imaging **30**(2), 243–250 (2011).
31. E. Gaudio, S. Chaberek, A. Montella, L. Pannarale, S. Morini, G. Novelli, F. Borghese, D. Conte, and K. Ostrowski, "Fractal and Fourier analysis of the hepatic sinusoidal network in normal and cirrhotic rat liver," J. Anat. **207**(2), 107–115 (2005).
32. K. E. Frisch, S. E. Duenwald-Kuehl, H. Kobayashi, C. S. Chamberlain, R. S. Lakes, and R. Vanderby, "Quantification of collagen organization using fractal dimensions and Fourier transforms," Acta Histochem. **114**(2), 140–144 (2012).
33. J. B. Florindo and O. M. Bruno, "Fractal descriptors based on Fourier spectrum applied to texture analysis," Phys. A **391**(20), 4909–4922 (2012).
34. L. Tian, B. Hunt, M. A. L. Bell, J. Yi, J. T. Smith, M. Ochoa, X. Intes, and N. J. Durr, "Deep learning in biomedical optics," Lasers Surg. Med. **53**(6), 748–775 (2021).
35. H.-C. Shin, H. R. Roth, M. Gao, L. Lu, Z. Xu, I. Nogues, J. Yao, D. Mollura, and R. M. Summers, "Deep convolutional neural networks for computer-aided detection: CNN architectures, dataset characteristics and transfer learning," IEEE Trans. Med. Imaging **35**(5), 1285–1298 (2016).
36. G. Wang, W. Li, M. A. Zuluaga, R. Pratt, P. A. Patel, M. Aertsen, T. Doel, A. L. David, J. Deprest, S. Ourselin, and T. Vercauteren, "Interactive medical image segmentation using deep learning with image-specific fine tuning," IEEE Trans. Med. Imaging **37**(7), 1562–1573 (2018).
37. T. H. Nguyen, S. Sridharan, V. Macias, A. Kajdacsy-Balla, J. Melamed, M. N. Do, and G. Popescu, "Automatic Gleason grading of prostate cancer using quantitative phase imaging and machine learning," J. Biomed. Opt. **22**(3), 036015 (2017).
38. N. Wu, J. Phang, J. Park, Y. Shen, Z. Huang, M. Zorin, S. Jastrzebski, T. Fevry, J. Katsnelson, E. Kim, S. Wolfson, U. Parikh, S. Gaddam, L. L. Y. Lin, K. Ho, J. D. Weinstein, B. Reig, Y. Gao, H. Toth, K. Pysarenko, A. Lewin, J. Lee, K. Airola, E. Mema, S. Chung, E. Hwang, N. Samreen, S. G. Kim, L. Heacock, L. Moy, K. Cho, and K. J. Geras, "Deep neural networks improve radiologists' performance in breast cancer screening," IEEE Trans. Med. Imaging **39**(4), 1184–1194 (2020).

Biomedical Optics EXPRESS

39. A. Imran, J. Li, Y. Pei, J.-J. Yang, and Q. Wang, "Comparative analysis of vessel segmentation techniques in retinal images," IEEE Access **7**, 114862–114887 (2019).
40. M. R. K. Mookiah, S. Hogg, T. J. MacGillivray, V. Prathiba, R. Pradeepa, V. Mohan, R. M. Anjana, A. S. Doney, C. N. Palmer, and E. Trucco, "A review of machine learning methods for retinal blood vessel segmentation and artery/vein classification," Med. Image Anal. **68**, 101905 (2021).